

# Chapter 11

## Doppler Tomography

Thomas R. Marsh and Axel D. Schwope

### 11.1 Introduction

The spectra of binary stars continually vary as the two stars orbit, but underlying this are two invariant spectra which simply shift in wavelength according to the changing radial velocities of their respective stars. In this case we know, or at least we can greatly restrict, the possible ways in which the radial velocities vary, and from a large set of observed spectra it becomes possible to deduce the individual stellar spectra, as is accomplished with the technique known as “spectral disentangling” ([46]; see Chap. 7). A different but related situation arises in accreting binary stars. Again the spectra continually change, and again, to a first approximation there is an underlying fixed pattern. However, in this case it is not so much the spectrum that we are interested in (it is usual to focus on individual atomic lines with presumed near delta-function intrinsic profiles), but the distribution of velocities of emission sites within the binary. It was this problem in the context of the emission line profiles from cataclysmic variable stars that led to the development of the method of Doppler tomography [30]. The complex variations of these stars have long been recognised, a good example being the star WZ Sge which shows strong line emission from the impact of the mass transfer stream with the accretion disc which traces an “S-wave” in the spectra trailed across photographic plates taken by Kraft et al. in the early 1960s [26]. Since its application to cataclysmic variable stars, Doppler tomography

---

T.R. Marsh (✉)

Department of Physics, University of Warwick, Coventry CV4 7AL, UK

e-mail: [T.R.Marsh@warwick.ac.uk](mailto:T.R.Marsh@warwick.ac.uk)

A.D. Schwope

Leibniz-Institute for Astrophysics Potsdam (AIP), An der Sternwarte 16, 14482 Potsdam, Germany

e-mail: [ASchwope@aip.de](mailto:ASchwope@aip.de)

has been applied to many other types of stars, but the same principle of a fixed rotating structure links them all.

In this chapter we describe the method, and recent variants of it, and then discuss significant results that have come from its application.

## 11.2 Principles of Doppler Tomography

In this section we present the principles underlying Doppler tomography. The reader is also referred to past reviews containing a pedagogical element for different perspectives on this topic which can be confusing on first encounter [9, 28, 29]. We begin by defining the coordinate system generally used.

### 11.2.1 Coordinates

In Doppler tomography, we usually work with images as a function of velocity coordinates, which introduces some subtleties as to the precise coordinate system being used. For instance, while one is used to spatial images of binary stars in “the rotating frame”, the velocity space coordinate frame used in Doppler images is *not* its direct equivalent. If it were, all emission from either star would be placed at zero velocity since the stars are fixed in the rotating frame. Therefore this section is devoted to a detailed explanation of the coordinates used to present Doppler maps and the reasoning behind the choices made.

For some target (usually an accreting binary star) under consideration, assume that there exists a uniformly rotating frame of reference  $F'$  in which the target’s brightness distribution remains constant. That is, the brightness at every point in this reference frame is unchanging, even if there is movement of material within it. Ideally we would like to know the distribution of emission sources in this frame, but, unfortunately the systems under study are far too small to be spatially-resolved and we have to fall back on more indirect methods. For binary stars in circular orbits,  $F'$  rotates with the two stars, and we will refer to it as “the” rotating frame, although other effects such as precession or spin of a magnetic accretor could serve to define it differently in some cases. Each point in  $F'$  has an associated position  $(x', y', z')$  and velocity  $(v'_x, v'_y, v'_z)$ , although note that material with very different velocities can exist at closely-spaced spatial positions, and there is not necessarily a simple translation between position and velocity in this or any other frame. Without loss of generality, we will take the rotation axis to be parallel to the  $z'$ -axis, the zero-point of time and phase to be the time when the  $x$ -axis points as close as it can to Earth (so that Earth at this time lies in the positive quadrant of the  $x'$ - $z'$  plane), and the  $y'$ -axis to be defined in accordance with a right-handed set of axes, i.e.  $\hat{\mathbf{y}}' = \hat{\mathbf{z}}' \wedge \hat{\mathbf{x}}'$ . In the case of binary stars we will also define the origin to be at the centre of one of the two stars and the  $x$ -axis to point towards its companion, usually from the accreting star to

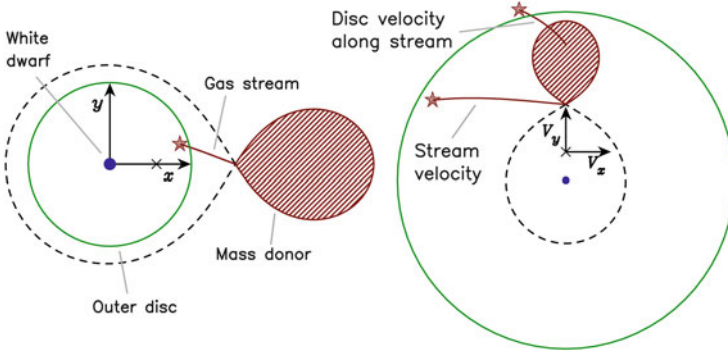


**Fig. 11.1** *Left:* a schematic representation of an accreting binary in spatial coordinates, showing the definition of the  $x$  and  $y$  axes described in the text. The binary rotates anti-clockwise in this representation. *Right:* the equivalent in terms of the inertial  $V_x, V_y$  coordinates discussed in the text. Any features in “solid body” rotation, such as the two stars and the Roche lobes, preserve their shapes but are rotated  $90^\circ$  anti-clockwise. The mass transfer stream is plotted in two ways, (a) the actual velocity of the stream (lower track), and (b) the Keplerian velocity of the disc along the track of the stream (upper). The solid circle marking the outer edge of the disc in the spatial representation on the left transforms to the outermost circle on the right, an inversion of radial ordering characteristic of velocity space Doppler maps. The rest of the disc lies even further out than the outermost circle. The binary rotates around the centre of mass, indicated by a ‘X’ on the  $x$ -axis of the left-hand figure, which is therefore the origin of the velocity space plot on the right. If the accretor spins faster than the binary, its emission would continue to be centred at the point indicated on the right-hand plot, but it would be more broadly distributed

the mass donor (see Fig. 11.1 for a visual representation). This means that the centre of the accreting star (star 1) will be located at  $(x', y', z') = (0, 0, 0)$ , the centre of the donor star (star 2) is at  $(a, 0, 0)$  where  $a$  is the binary separation, while the centre of mass is at  $\mathbf{C} = (\mu a, 0, 0)$ , where  $\mu = M_2/(M_1 + M_2)$ , with  $M_1$  and  $M_2$  the two stellar masses. By definition in this case, the two stars are fixed within the rotating frame and have velocity  $(0, 0, 0)$ , but we view the system from the (approximately) inertial frame of Earth, and need to transform the velocity to see what we observe. It is simplest to translate to the Earth’s frame via an intermediate inertial frame  $F$  defined as the inertial frame that is instantaneously aligned with the rotating frame  $F'$  at any particular time. In other words, at any given orbital phase  $F$  is defined by the orientation of the  $F'$  axes. This leads to the following transformations between the position  $\mathbf{r}'$  and velocity  $\mathbf{v}'$  in  $F$  to the position  $\mathbf{r}$  and velocity  $\mathbf{v}$  in  $F$ :

$$\mathbf{r} = \mathbf{r}', \tag{11.1}$$

$$\mathbf{v} = \mathbf{v}' + \boldsymbol{\Omega} \wedge (\mathbf{r}' - \mathbf{C}), \tag{11.2}$$

where  $\boldsymbol{\Omega} = \Omega \hat{\mathbf{z}}$  is the angular velocity characterising the rotating frame. By assumption, a given point in the rotating frame  $F'$  has a fixed value of  $\mathbf{r}'$  and  $\mathbf{v}'$ . Since  $\Omega$  is also constant then so too are  $\mathbf{r}$  and  $\mathbf{v}$ . Doppler maps as usually presented

are maps of emission line intensity as a function of  $\mathbf{v}$  as defined by Eq. 11.2, i.e.  $I(\mathbf{v})$ .<sup>1</sup>

Applying the above relation to the centre of mass of the donor star which has  $\mathbf{r}' = (a, 0, 0)$  and  $\mathbf{v}' = (0, 0, 0)$ , gives  $\mathbf{v} = (0, a(1 - \mu)\Omega, 0)$ , so if the donor star emits, it contributes at a point on the positive  $y$  axis in velocity-space, which is a characteristic and important feature of Doppler maps. Given the definition of  $F$ , it is not one inertial frame but a set of inertial frames that maintains alignment with the rotating frame of the system, and therefore the “constant” vector  $\mathbf{v}$  steadily rotates with respect to us. Spectroscopy via the Doppler effect leaves us sensitive only to its component along our line of sight or “radial velocity”  $V_R$  which is straightforwardly shown to be

$$V_R = \gamma - v_x \sin(i) \cos(2\pi\phi) + v_y \sin(i) \sin(2\pi\phi) - v_z \cos(i),$$

with the various signs the result of the standard choice of a positive sign for the radial velocity for objects receding from Earth. Here,  $\gamma$  is the “systemic velocity” or radial velocity of the centre of mass of the system (assumed fixed),  $\phi$  is the orbital phase (from 0 to 1) and  $i$  is the inclination of the orbital axis with respect to the line of sight (assumed fixed). An edge-on, eclipsing system is characterised by  $i = 90^\circ$ . Except for eclipsing systems, we usually have little idea of  $i$ , which leaves Doppler maps degenerate to changes in  $i$  which stretch and compress the three axes through the  $\sin i$ ,  $\cos i$  factors if we use  $v_x$ ,  $v_y$ , and  $v_z$  as our coordinates. Therefore we instead subsume the  $\sin i$  and  $\cos i$  factors into the coordinates to give instead

$$V_R = \gamma - V_x \cos(2\pi\phi) + V_y \sin(2\pi\phi) - V_z, \quad (11.3)$$

where  $(V_x, V_y, V_z) = (v_x \sin i, v_y \sin i, v_z \cos i)$ . Equation 11.3 is the origin of Kraft’s “S-waves” [26] and is fundamental to Doppler imaging. As has been shown, a fixed point in the rotating frame  $F'$  corresponds to a fixed point in  $F$  which has a unique set of velocity coordinates  $(v_x, v_y, v_z)$ . The Doppler effect introduces an extra uncertainty due to projection effects, but Eq. 11.3 shows that if we measure  $V_R$  as a function of orbital phase and fit a sinusoid plus a constant, we can deduce accurate values for the closely-related triad,  $(V_x, V_y, V_z)$  (assuming we know  $\gamma$ ). It is worth remarking at this point that although the final coordinate system is related to the instantaneous frame  $F$  by a modest scaling transformation, if we want to get back to the rotating frame  $F'$ , we need to invert Eq. 11.2 which requires that we know  $i$ ,  $\mu$  (or equivalently  $q = M_2/M_1$ ) and  $\mathbf{r}$  as well. We can in some cases learn  $i$  and  $q$ , but in most cases we have very little purchase on the spatial position which does not enter Eq. 11.3 at all. There is thus little reason to try to effect this transformation. The same information is needed to obtain emissivity as a function of spatial position  $\mathbf{r}$ , and so it is similarly rare to compute spatial Doppler maps.

<sup>1</sup>With a slight scaling due to projection effects as will be discussed.

In the final  $(V_x, V_y, V_z)$  coordinates the centre of donor star is placed at  $(0, a(1 - \mu)\Omega \sin(i), 0)$ , which is on the  $V_y$  axis with ordinate  $(M_1/(M_1 + M_2))\Omega a \sin(i) = +K_2$ , the standard semi-amplitude one would measure from a radial velocity measurement of the donor star. Similarly, emission from the accretor is centred on  $(0, -K_1, 0)$ . The shapes of the components plotted in Fig. 11.1 are entirely defined by  $K_1$  and  $K_2$  alone, which fix the scale and relative sizes of the components. This is the advantage of subsuming the projection factors  $\sin(i)$  and  $\cos(i)$  into the coordinates as then, if one is lucky,  $K_1$  and  $K_2$  can be directly read from the map just by measuring how far corresponding features are from the origin.

### 11.2.2 3D Profile Formation

From the previous section it is clear that a spot of emission leads to a sharp emission line which varies sinusoidally in radial velocity with time. If we saw such a feature we could associate the strength of the component with a particular point  $(V_x, V_y, V_z)$  in velocity space, a very crude “image”. To go further we need to consider a continuous distribution of emission, so suppose that we have a distribution of emissivity so that

$$I(V_x, V_y, V_z) dV_x dV_y dV_z,$$

is the flux at Earth (units of power per unit area) from an infinitesimal cuboid in velocity space defined by  $V_x$  to  $V_x + dV_x$ ,  $V_y$  to  $V_y + dV_y$ , and  $V_z$  to  $V_z + dV_z$ . This flux will appear centred at radial velocity  $V_R$  given by Eq. 11.3, but it will be somewhat broadened by processes intrinsic to the source, such as thermal broadening, and also by instrumental broadening. For simplicity we assume that these can be represented by a single broadening profile  $g(V)$  that satisfies

$$\int_{-\infty}^{+\infty} g(V) dV = 1.$$

In this case the line profile that will be observed is given by

$$f(V, \phi) = \int_{-\infty}^{+\infty} \int_{-\infty}^{+\infty} \int_{-\infty}^{+\infty} I(V_x, V_y, V_z) g(V - V_R) dV_x dV_y dV_z, \quad (11.4)$$

with  $V_R$  given by Eq. 11.3. The profile  $f$  as defined here has units of power per unit area per unit velocity interval. Doppler tomography is only effective if the broadening function  $g$  is relatively narrow compared to the width of the emission region. In the ideal case,  $g(V) = \delta(V)$ , a delta-function, and Eq. 11.4 can be viewed as selecting a nested set of surfaces in three-dimensional velocity space defined by the condition  $V = V_R$  with the surfaces labelled by the particular velocity  $V$  in the

profile to which they contribute. Since Eq. 11.3 can be written as

$$aV_x + bV_y + cV_z = d, \quad (11.5)$$

where  $a = -\cos(2\pi\phi)$ ,  $b = +\sin(2\pi\phi)$ ,  $c = -1$  and  $d = V - \gamma$  all constants for a particular phase  $\phi$ , we can see that the surfaces are in fact a set of parallel planes.

The profile formation encapsulated in Eq. 11.4 converts a 3D distribution of emission into a 2D function and information is certainly lost. Unique inversion from 2D line profiles to a fully 3D Doppler image is not possible, even though as we saw with the discussion of a single spot in the previous section, some 3D information is encoded in the profiles through the mean velocity of S-waves [2, 29]. This has been used in some studies of Algol systems [1, 33, 34] and its potential for polars has been explored [25], but not so far applied. Since this review is focussed on cataclysmic variable stars we do not discuss it further but refer the interested reader to the cited studies. With the extra condition that the image is two-dimensional in form, there results the conventional 2D Doppler tomography used in the majority of published Doppler maps, and we turn to this now.

### 11.2.3 2D Profile Formation

The solid-body rotation term of Eq. 11.2,  $\boldsymbol{\Omega} \wedge (\mathbf{r} - \mathbf{C})$ , only leads to velocities parallel to the  $x$ - $y$  orbital plane of the system. As the result of strong symmetry between  $+z$  and  $-z$ , it is often the case that bulk motions within the rotating frame are also largely parallel to the orbital plane. This applies to the commonly-seen mass transfer stream and accretion disc components for instance. This means that in many instances one can assume that there is only significant emission close to  $V_z = 0$ , allowing us to integrate out the  $z$ -component and leaving

$$f(V, \phi) = \int_{-\infty}^{+\infty} \int_{-\infty}^{+\infty} I(V_x, V_y) g(V - V_R) dV_x dV_y, \quad (11.6)$$

(see Eq. 5 in [28]). The set of planes in 3D defined by Eq. 11.5 then becomes a set of lines in 2D:

$$aV_x + bV_y = d. \quad (11.7)$$

Given the values of the coefficients  $a$  and  $b$ , the lines at orbital phase  $\phi$  run parallel to the direction  $\mathbf{P} = (\sin 2\pi\phi, \cos 2\pi\phi)$ . The profile of Eq. 11.6 can thus be thought of as a ‘‘projection’’ (or collapse) of the 2D image along the direction defined by  $\mathbf{P}$ , a direction that rotates clockwise as the orbital phase advances, which can be thought of as the direction that the Earth rotates as seen from the rotating frame of the binary.

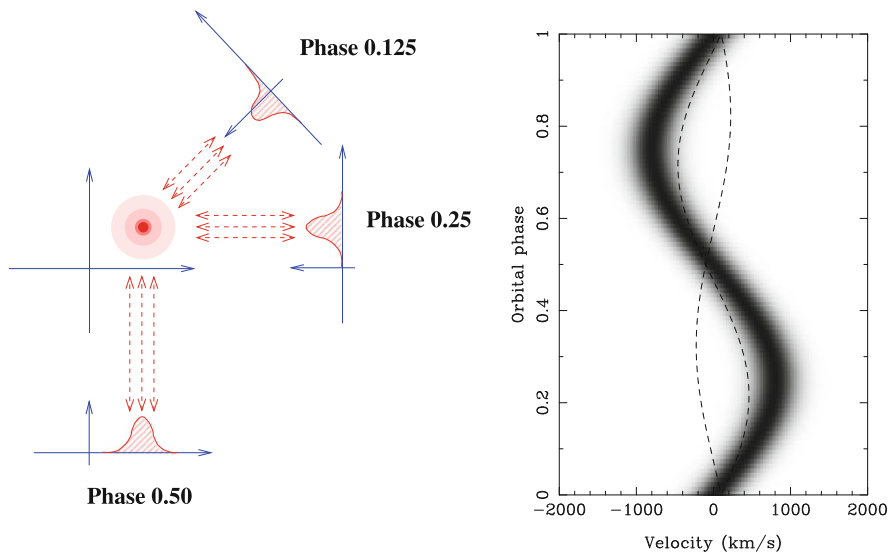


**Fig. 11.2** *Left*: a spot in velocity-space with corresponding line profiles at three orbital phases which are the projections of the image in the directions shown. In reverse if the profiles are smeared along the same directions, a process called “back-projection”, they will add together at the position of the spot. *Right*: a “trailed” spectrum with profiles plotted as a 2D image with phase ascending corresponding to the image on the *left*. Back-projection in this dataspace corresponds to line integrals along multiple paths (Re dashed lines show two examples); paths that coincide with the S-wave lead to a large intensity at the corresponding  $(V_x, V_y)$  position (Figure from [28])

To emphasise these points here is Eq. 11.6 written with the  $V_R$  term expanded and the broadening function set to a  $\delta$ -function:

$$f(V, \phi) = \int_{-\infty}^{+\infty} \int_{-\infty}^{+\infty} I(V_x, V_y) \delta(V - \gamma + V_x \cos 2\pi\phi - V_y \sin 2\pi\phi) dV_x dV_y. \tag{11.8}$$

Figure 11.2 is an attempt to visualise this relation. On the left, the profiles equivalent to a single spot of emission are displayed at the correct projection direction for three different phases. On the right, the result of measurements at many phases are plotted as a greyscale running up the page, a plot known as a “trailed spectrum” in deference to the process of trailing objects along the slits of spectrograph that was employed when observing such objects in the days of photographic plates.

### 11.2.4 Inversion

The profile formation encapsulated in Eqs. 11.6 and 11.8 means that a series of line profiles taken at different phases around a binary orbit is the equivalent of a series

of projections of a 2D image along straight lines into 1D. This is mathematically identical in form to the use in medicine of a series of X-ray images taken at different angles to image the interior of the human body. Such X-ray photographs are imaged with a method known as computerised tomography, where the word “tomography” is connected to the reconstruction of images from projections. This led to Doppler tomography [30].

#### 11.2.4.1 Filtered Back-projection

A series of projections can be inverted to produce an image in a two-stage linear process called filtered back-projection [28, 30]. In the context of Doppler tomography, first of all a filter is applied in velocity to each line profile to produce modified profiles  $\tilde{f}(V, \phi)$ . In Fourier space the filter boosts the amplitudes of high frequencies (frequencies in the sense of cycles per step in velocity). This is a simple and fast process, although some care is needed to avoid over-amplification of noise which usually dominates at the very highest frequencies. The next step is back-projection:

$$I(V_x, V_y) = \int_0^{0.5} \tilde{f}(\gamma - V_x \sin 2\pi\phi + V_y \sin 2\pi\phi, \phi) d\phi, \quad (11.9)$$

which can also be written in a way that resembles Eq. 11.8 as

$$I(V_x, V_y) = \int_0^{0.5} \tilde{f}(V, \phi) \delta(V - \gamma + V_x \sin 2\pi\phi - V_y \sin 2\pi\phi) d\phi.$$

Figure 11.2 contains two means of visualising this relation. On the left, the approximate inverse of profile formation by projection is instead to smear each profile back along the original projection direction, as indicated by the double-direction arrows. Where multiple streaks reinforce, a spot will form. This is why the process is called back-projection. The right-hand panel shows a more literal interpretation of the equation as a series of integrals along sinusoidal paths in a trailed spectrum over the data. When the path of such an integral runs along an S-wave, a strong contribution will emerge resulting in a spot.

Although not often used in practice, the concept of back-projection is a very helpful one for interpreting Doppler images. For instance it is clear that bad pixels, perhaps the result of cosmic rays, will lead to the appearance of linear features in maps, and caution should always be exercised if such features are apparent.

#### 11.2.4.2 Regularised Fitting

It is more common to regard Doppler imaging as a model fitting problem. One represents the map by (usually) a square grid of pixels covering the necessary range



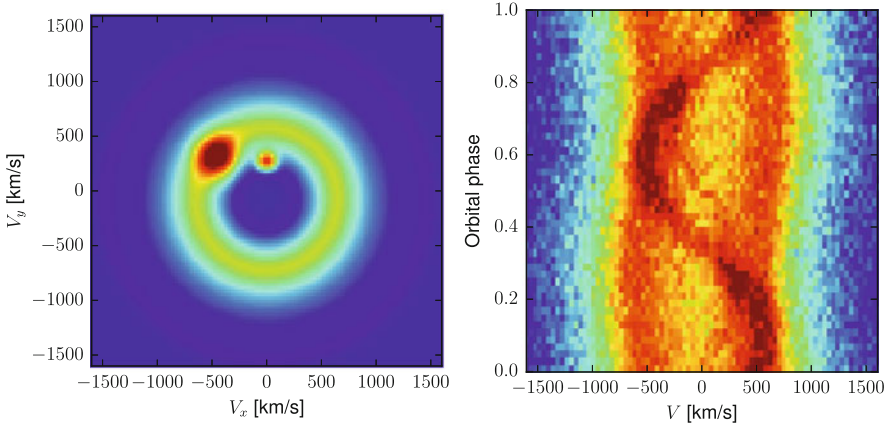


**Fig. 11.3** *Left*: an artificial generated Doppler map including a component to represent a disc (ring-like structure), a gas stream/disc impact spot (left-hand bright spot), and a weak spot from the donor star. *Right*: data generated from the model with added pseudo-random gaussian white noise

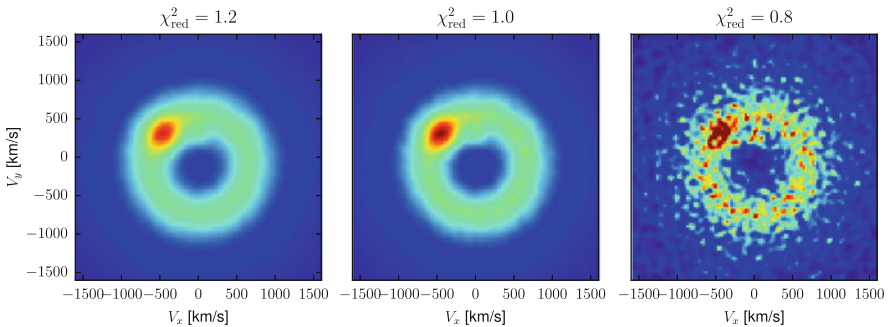


**Fig. 11.4** Three image reconstructions from the data of Fig. 11.3, differentiated by the  $\chi^2$  per data point reached in each case. All are plotted to the same maximum intensity used to display the model in Fig. 11.3 to which they should be compared. Note the marginal signs of emission from the donor star, which is in accord with its level in the data of Fig. 11.3

of velocities with enough resolution to match the data, and then asks the question “what set of pixel intensities best matches the data?”. The immediate problem one faces is that if “best” is regarded as the minimum  $\chi^2$ , the usual answer is a useless mass of high and low values dominated by noise. To show this, in Fig. 11.3 we show an artificial image and some data computed from it with added pseudo-random gaussian white noise. Two spots representing the gas stream/disc impact region and emission from the donor star have been added as features commonly seen in real data. In Fig. 11.4 we show three reconstructions from the data of Fig. 11.3 for different values of  $\chi_{\text{red}}^2 = \chi^2/N$ , with  $N$  set to the number of data points rather than the number of degrees of freedom, the latter being difficult to define in this case.

None of the reconstructions shown are at the minimum  $\chi_{\text{red}}^2$  which turns out to be  $\sim 0.68$  in this case, but already noise is overwhelming the reconstructed image in the right-hand plot of Fig. 11.4.

Figure 11.4 shows that aiming for minimum  $\chi^2$  is a bad idea, but for any threshold value of  $\chi^2$ ,  $T > \chi_{\text{min}}^2$  above the minimum, there is usually an infinity of possible images that can reach the range  $T \geq \chi^2 \geq \chi_{\text{min}}^2$ , and we need some criterion to select between them. This is answered by “regularisation” where instead of minimising  $\chi^2$ , one minimises  $\chi^2 - \lambda S$  where  $S$  is some function of the image that is maximum for “good” images, independent of the data, and  $\lambda$  is a positive parameter (Lagrangian multiplier) that sets the relative importance of minimising  $\chi^2$  versus maximising  $S$ . (Equally one can minimise  $\chi^2 + \lambda S'$  if *minimum*  $S'$  selects the best images.) In the 1988 paper introducing Doppler tomography [30],  $S$  was chosen to be a measure of image “entropy”, hence “maximum entropy”, reflecting to large degree inheritance from its use in the method of eclipse mapping developed by [17], but other measures can easily be imagined, for instance measures of maximum local smoothness, and may indeed have advantages in practice [57].

Figure 11.4 shows that there is no unique inversion, as there is a trade-off between noise and goodness of fit. In this case the particular solution selected is labelled by the  $\chi^2$  achieved. As this is lowered, one moves from a solution of large  $\lambda$  where  $S$  is more influential to one of small  $\lambda$  where  $\chi^2$  dominates. The choice of where to stop is really one of taste: most would agree that the right-hand image of Fig. 11.4 has been pushed too far, whereas the left-hand image looks overly smooth. The precise values of  $\chi^2$  and  $S$  vary from case to case, but there is usually a significant range of values over which the qualitative conclusions one draws from an image do not change, even if the detailed level of apparent noise may vary.

The noise–smoothness trade-off is not specific to regularised fitting, but applies to filtered back-projection too where one must set a parameter to limit the amplification of high-frequency noise when filtering. A possible alternative method to approach the problem would be to parameterise the problem by describing the disc through a small number of components, and then one could simply fit for the unique solution of minimum  $\chi^2$ . This is a method that has achieved some success in the case of fitting the light curves of eclipsing dwarf novae for example [18, 39]. Many observed Doppler maps can be described in terms of a disc plus one or two spots, so such a method may be possible, but would run the risk of missing unexpected structures, and is probably not a good avenue to pursue.

### 11.2.5 Doppler Tomography Extras

There are a number of additional effects that one can allow for when using Doppler tomography which we briefly discuss here.

### 11.2.5.1 Systemic Velocity

We have already referred to 3D imaging that can cope with a range of  $V_z$  values. This has the advantage of automatically allowing for the systemic velocity  $\gamma$  which simply displaces the image in the  $V_z$  direction (see Eq. 11.3). In 2D imaging we assume  $V_z = 0$  and therefore it is important to use the correct value for the systemic velocity  $\gamma$ . If not, the resultant image will be blurred, as discussed in [30]. If no independent value for  $\gamma$  exists, the standard approach is to optimise  $\gamma$  through minimisation of  $\chi^2$  during the imaging cycle. This is generally a fast operation.

### 11.2.5.2 Orbital Phase Uncertainty

In non-eclipsing systems, without clear donor stars it can be difficult to know the absolute orbital phase. This leads to a rotational uncertainty in the resultant image that must be considered when interpreting it. In the case of cataclysmic variables, the emission line radial velocities are often used as a proxy for the white dwarf although it has been known for many years that they are very often not reliable, and that the orbital phase zero point that one deduces from emission lines tends to lag the true zero phase [56]. This causes an anti-clockwise rotation of a Doppler map based upon an emission-line phase. As a consequence, a bright-spot component for instance will appear lower in the map than expected. Caution is needed if such an effect is seen; the problem is most severe in short-period systems where the white dwarf's radial velocity semi-amplitude is small.

### 11.2.5.3 Finite Exposures

For faint and very short period systems, it can be difficult to acquire spectra in a time much shorter than the orbital period. Consider for instance the 21-st magnitude 5-min binary HM Cnc where it is a challenge even to take exposure in less time than the binary takes to complete an entire orbit [37]. This leads to azimuthal smearing of the Doppler map by an amount  $2\pi \Delta t/P$  radians where  $\Delta t$  is the exposure time and  $P$  the orbital period. Whether this is significant depends upon the intrinsic width of the line profile and the instrumental resolution. A feature  $K$  km/s from the origin of the map will be smeared in azimuth by  $2\pi K \Delta t/P$ , and particularly when planning observations, it is good to consider how this compares to the spectrograph velocity resolution,  $c\Delta\lambda/\lambda$ , for instance. Blurring can be combatted by de-convolution, and in the code used by [30] (see below), one can compute models allowing for finite exposures, which can be helpful in sharpening bright-spot features in difficult cases.

### 11.2.5.4 Blended Lines

It is fairly common to encounter blended (overlapping) lines. In the case of AM CVn stars, HeII 4686 is only separated by  $\sim 1700 \text{ km s}^{-1}$  from HeI 4713, and similarly the Ca II triplet lines in the *I*-band each have a nearby line of the Paschen series that can be significant. In such cases it is straightforward within the regularised fit approach to allow for multiple lines, perhaps with independent images or as scaled versions of the same image. In practice this rarely works perfectly, and particularly in the weaker member of a blend, it is common to see ring-like features resulting from the nearby stronger line. Still, the results are improved over simply ignoring the effect.

### 11.2.5.5 Modulation Mapping

Standard Doppler tomography produces a map that can be regarded as an orbitally-averaged image, although strictly speaking one of the “axioms” of standard Doppler tomography is that the image does not change [28]. In reality there are almost always geometric effects which lead to a break-down of this assumption. Most obviously for instance, emission on the heated face of the donor star will move into and out of our sight as the binary rotates. In the modulation mapping method introduced by [51], one regards the image as a Fourier series in orbital phase:

$$I(V_x, V_y) = I_0(V_x, V_y) + A(V_x, V_y) \cos 2\pi\phi + B(V_x, V_y) \sin 2\pi\phi.$$

The reconstruction then finds  $I_0$ , as well as the cosine and sine components  $A$  and  $B$ . This has some value in interpreting the sharp emission components and can deliver greatly improved fits to the data [4].

## 11.2.6 Codes for Doppler Tomography

We finish this section with a brief description of three publicly-available codes that we are aware of for implementing Doppler tomography. The original maximum entropy code using the MEMSYS algorithm [47] is available as an add-on<sup>2</sup> to the STARLINK software suite. Its chief disadvantage is probably the learning curve that must be surmounted if one is unfamiliar with STARLINK. Henk Spruit distributes a simple maximum entropy-based code<sup>3</sup> that is straightforward to get going, although it misses some of the features of the original code, such as dealing with blended lines. Finally, a recent variant using a different regularisation measuring

<sup>2</sup><http://www.astro.warwick.ac.uk/people/marsh/software/>

<sup>3</sup><http://www.mpa-garching.mpg.de/~henk/>

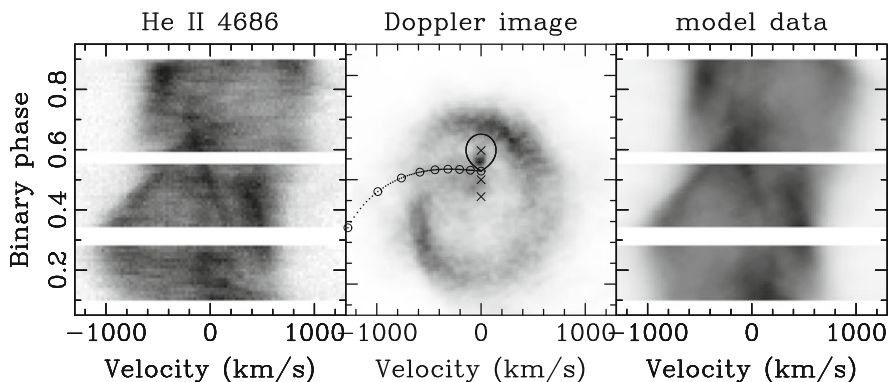


Fig. 11.5 Spiral shock structures seen in the dwarf nova IP Peg during outburst [14]

the variation across an image has been developed [57] and is available for general use.<sup>4</sup> An advantage of the regularisation function chosen is that it copes naturally with negative image values. Although these should not occur in theory, in practice absorption effects, particularly in highly-inclined systems, often lead to a need for negative image values which are tricky to accommodate with entropy-based codes.

## 11.3 Doppler Tomography in Practice

Doppler tomography has achieved the status of a standard tool of the field and, with over 400 citations to the original paper [30] and many others besides, it is not possible to cover all of the results that have come from its application. In this section therefore we concentrate upon some highlights, particularly those where it has led to insights that were not obvious from the data alone.

### 11.3.1 *Spiral Shocks*

Coming only a decade after the development of the method, the discovery of global spiral structures in the accretion disc of the dwarf nova IP Peg [53] is still a stand-out result from the application of Doppler tomography. Very complex profile variations (Fig. 11.5) in which the classic double-peaks from the accretion disc appear to show discontinuities, were only convincingly interpreted after they were mapped. Similar variations have been seen in a number of other systems [3, 12, 20] and are thought to be induced by the tidal potential of the binaries.

<sup>4</sup><http://home.hiroshima-u.ac.jp/~uemuram/dttvm/>

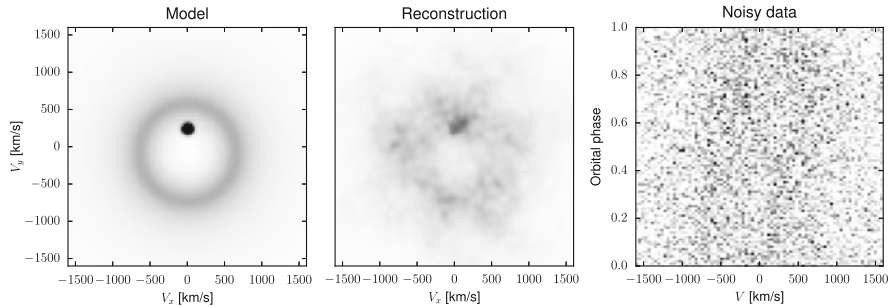


**Fig. 11.6** A simulation of a faint system with emission from a donor. Even though the donor is barely visible in the data on the *right*, a significant excess appears at its location in the reconstruction

### 11.3.2 Donor Star Emission

In many short period cataclysmic variable stars and low-mass X-ray binaries it is practically impossible to obtain reliable radial velocity measurements of the compact object because it has a low amplitude and one has to use very broad emission lines as a proxy for the object itself. In these cases, detection of the donor can be very useful indeed for the precise phase constraint that it can return as well as the constraint it places upon the mass of the compact object. Doppler tomography can be a useful detection method here. Figure 11.6 shows a simulation where significant emission from the donor can be recovered in a map even though it is impossible to see in the trailed spectrum. This has been put to good use in the case of X-ray binaries using Bowen fluorescence emission (C III/N III 4640) from the donor [6, 52], and using Balmer and Ca II emission to reveal brown dwarf-mass donors in cataclysmic variable stars [42, 55, 58]. The last cited work reveals a further interesting feature (Fig. 11.7), namely that Ca II emission reveals the donor with particular clarity in some cases, and is also distinctly sharper when it comes from the disc. There is a distinct impression that the Balmer line map ( $H\beta$ ) is limited by significant intrinsic line broadening. For other examples of donor stars in Doppler maps see Sect. 11.4.3.

### 11.3.3 AM CVn Stars

Over the past decade there have been many new discoveries of the hydrogen-deficient accreting binaries known as AM CVn stars. The line profiles of these systems are unusual for sometimes featuring emission from the white dwarf [27, 31]. The position of this emission in Doppler maps along with the position of the stream/disc impact spot has been used to constrain the system parameters in some of these systems [36] in which no donor star has ever been directly detected. Doppler

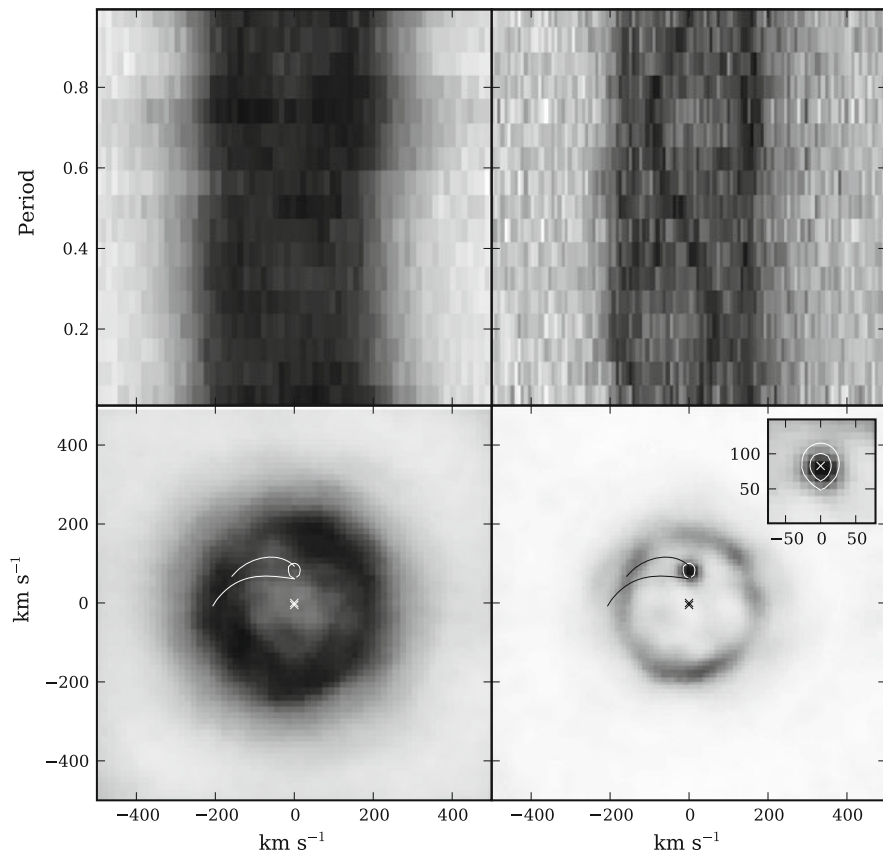


**Fig. 11.7**  $H\beta$  (left) and  $Ca\ II\ 8662$  (right) trailed spectra and Doppler images of the low-inclination dwarf nova GW Lib [58]. Emission from the donor star is particularly clear in  $Ca\ II$  emission

maps of AM CVn stars often also feature emission spots in unusual locations (see Fig. 11.8) which have yet to have had a convincing explanation. AM CVn systems have extreme mass ratios leading to low radial velocity amplitudes for the white dwarf. This makes the bright-spots (“S-waves”) particularly significant in measurement of their orbital periods. This has led to the use of Doppler maps for period measurement by through alignment of bright-spots over multiple nights of data [35].

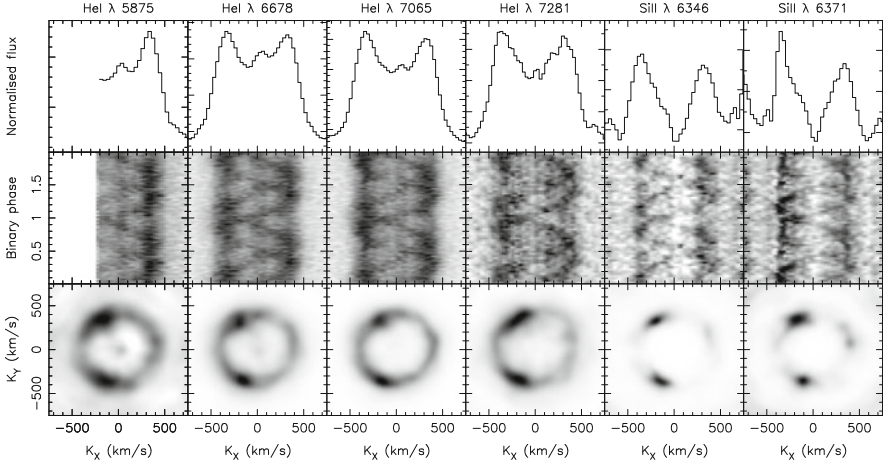


**Fig. 11.8** Doppler maps of the AM CVn star SDSS J124058.03-015919.2 show weak emission from the white dwarf (spot at low velocity), a spot at the standard stream/disc impact region in the *upper-left quadrant*, but also an unexplained component in the *lower-left quadrant*, and possibly even a third component on the right-hand side [35]

## 11.4 Doppler Tomography of Polars: Accretion Streams, Accretion Curtains and Half Stars

The last section of this chapter is devoted to a more detailed description of the achievements, main results but also the limitations of Doppler tomography applied to a specific class of close binaries, the polars.

Polars are cataclysmic binaries where accretion is dominated by strong magnetic fields of the white dwarf stars. The magnetic moment and the Alfvén radius of the accreting white dwarf are so large that both stars of the binary are kept in synchronous rotation; no accretion disc is formed. Instead matter is transferred to the white dwarfs via accretion streams and similar structures. The gravitational energy of the instantaneously accreted matter is released in small regions (spots, arcs) via X-ray bremsstrahlung, optical cyclotron radiation and an intensive radiation component in the UV/EUV spectral regime. While the former may deposit its energy in the irradiated hemisphere of the mass-donating late-type star (and distort its radial velocity curves), the latter is responsible for photoionisation of gaseous matter in the binary system. Recombination radiation from streaming and orbiting matter in the binary gives rise to the very complex and ever-changing line profiles that were impossible to disentangle with ‘classical’ methods like line-profile and radial-velocity fitting (see [19] for a photographic trailed spectrogram of the 81 min binary EF Eri).

The first ever tomogram of a magnetic CV, an H $\alpha$  map of the high-inclination system VV Pup, was published by [8] who noticed the fundamental difference of their Doppler map to those of non-magnetic CVs.



### 11.4.1 Accretion Streams and Curtains

The main features that are typically found in trailed spectrograms and Doppler maps of polars are highlighted in Fig. 11.9. The original data that were obtained with integration times between 20 and 60 s and covering several orbital cycles of the  $P_{\text{orb}} = 125$  min eclipsing binary were phase-averaged and arranged as pseudo-trailed spectrograms in the left column of the Figure. The emission lines belong to ionised Helium ( $\text{HeII}\lambda 4685$ ). Their existence immediately point to the presence of an ionising source (the ionisation potential of Helium is 54 eV) on the white dwarf. The recombination lines of the H-Balmer series and of neutral Helium show very similar features, the H-Balmer lines, however, typically show a larger optical thickness and their line width is broader. Their Doppler maps are less structured and therefore more difficult to interpret.

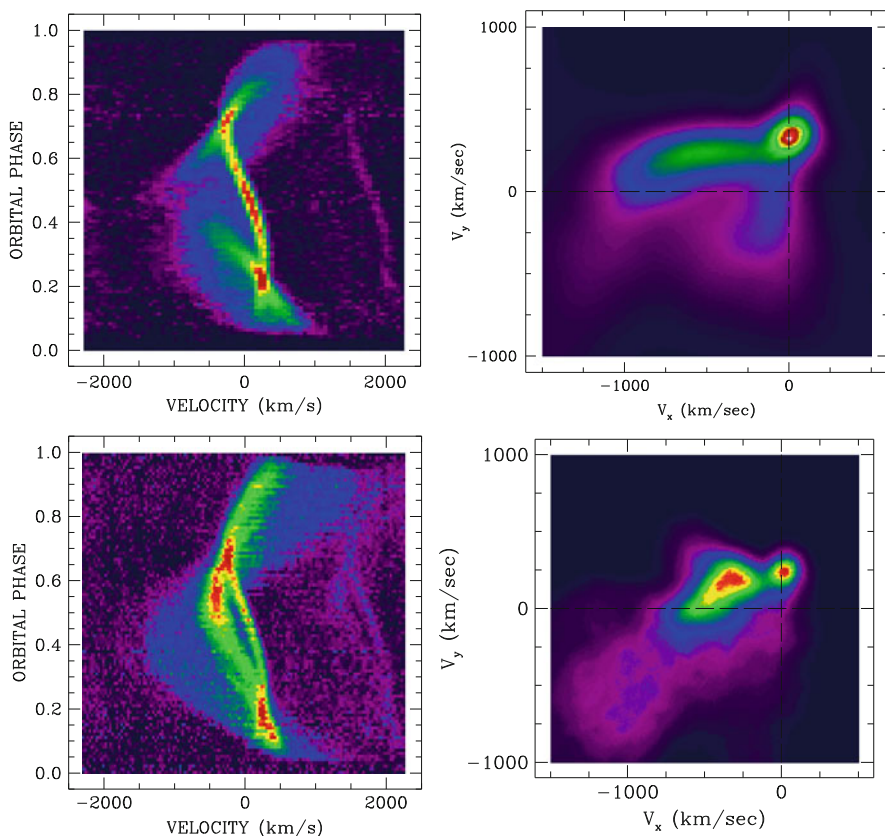


**Fig. 11.9** Trailed spectrograms of  $\text{HeII}\lambda 4685$  and Doppler maps of the  $P_{\text{orb}} = 125$  min eclipsing polar HU Aqr. The *top row* shows results obtained in the 1993 high accretion state, the *bottom row* those of the 1996 state of intermediate accretion (Adapted from [44, 45])

The trailed spectrograms show an S-wave best visible around phase 0.5. At this phase it has zero velocity and its radial velocity changes from being redshifted to become blueshifted. This narrow emission line (NEL) traces the mass-donating star (see Sect. 11.4.3 for a more detailed description of its properties).

Without tomography researchers were disentangling the line profiles into three or four Gaussians that were traced throughout the orbital cycle or only parts of it. The relative phasing, velocity amplitudes and widths of those components were used to locate their origin in different parts of the accretion stream and were used to imply considerable structure of the line-emitting gaseous matter (see, e.g., [38]).

The Doppler maps of the data reveal such divisions to be artificial. The high-state map (upper right) shows three main structures, a point-like spot of emission at  $(v_x, v_y) \simeq (0, 300) \text{ km s}^{-1}$ , a comet-like tail attached to it that extends to large negative velocities in the  $x$ -direction, and a more symmetric structure in the lower left quadrant, i.e. mainly at negative  $x$ - and  $y$ -velocities. If a trailed spectrogram is regarded as the projection of a velocity map onto the observers frame one understands that a structure like the long-tail generates a rather narrow emission line at phases 0.25 and 0.75 and a very broad line of width  $1000 \text{ km s}^{-1}$  at phases 0 and 0.5. This insight was only possible by Doppler tomography and it clearly limits any interpretation of Gaussian-deconvolved line profiles.

The structures in the Doppler map of Fig. 11.9 (top right) are interpreted quite naturally as originating from the donor star, the ballistic accretion stream falling freely in the gravitational potential of the white dwarf and the magnetically guided part of the stream. Figure 11.10 helps to reach a basic understanding of structures in polars. The choice of the coordinate system etc. follows the convention explained above (see Fig. 11.1). It is important to emphasise that the diagram to the right shows

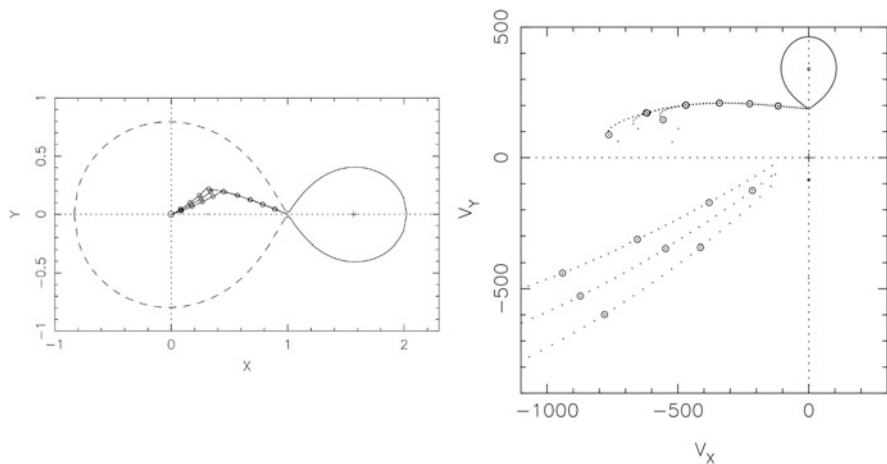


**Fig. 11.10** Accretion geometry of a polar in spatial (*left*) and Doppler coordinates (*right*). The inclination of the dipole axis with respect to the rotation axis is  $15^\circ$  and points towards the donor star

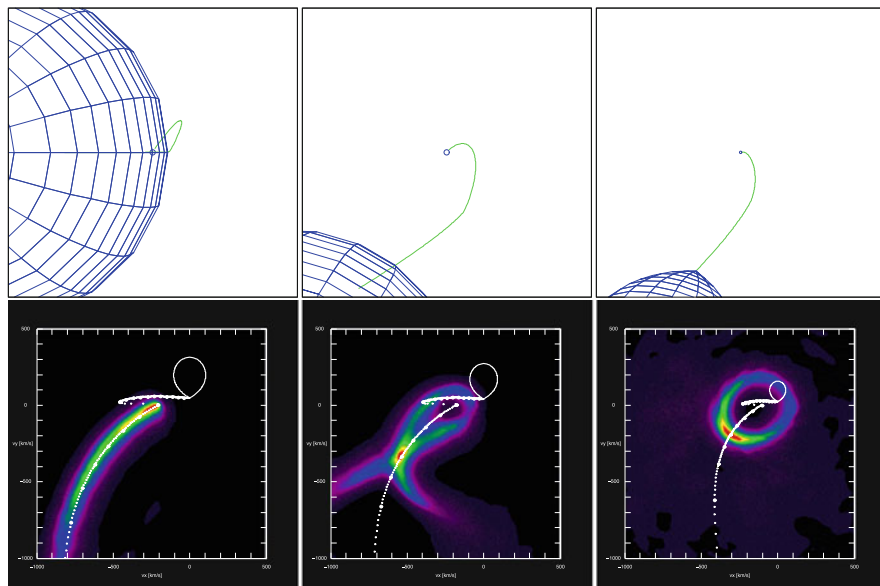


**Fig. 11.11** Effect of finite  $v_z$  component on Doppler maps for  $i = 30^\circ, 60^\circ,$  and  $90^\circ$  [49]

velocity projections onto the orbital plane because the streaming matter may have large velocities perpendicular to it. Non-zero streaming velocities out of the plane may have significant impact on the Doppler maps of low-inclination systems.

The adverse effect of non-zero  $V_z$ -velocities is illustrated in Fig. 11.11. A numerical experiment was set up in the following way. Matter freely falling along a dipolar field line was assumed to emit optically thin radiation in a non-specified atomic line. Each element along the trajectory from a coupling region towards the white dwarf was assumed to radiate away the same amount of energy. The components of the 3D velocity vectors were projected onto the observers frame as a function of the phase angle. The resulting trailed spectrogram was used to generate the Doppler maps shown in the bottom row of the figure for orbital inclinations of  $90^\circ, 60^\circ,$  and  $30^\circ$  (from left to right). While the emission lines for the  $90^\circ$  case are mapped exactly on the expected trajectory, fish- and ring-like maps emerge if the inclination angle is smaller. The largest brightness is still observed somewhere on the single-particle trajectory but the constant presence of blue- and red-shifted emission line components from the rising and falling parts along the field line leads to a map with emission in all four quadrants.

This example just illustrates the possible consequences of violating one of the basic assumptions (“axioms”) of Doppler tomography that all motion is parallel to the orbital plane.

Let’s come back to the Doppler map of HU Aqr obtained in the 1993 high accretion state (Fig. 11.9, top right). It seems as if there were two features whose locations in the map are influenced (to say the least) or are even fixed by the masses

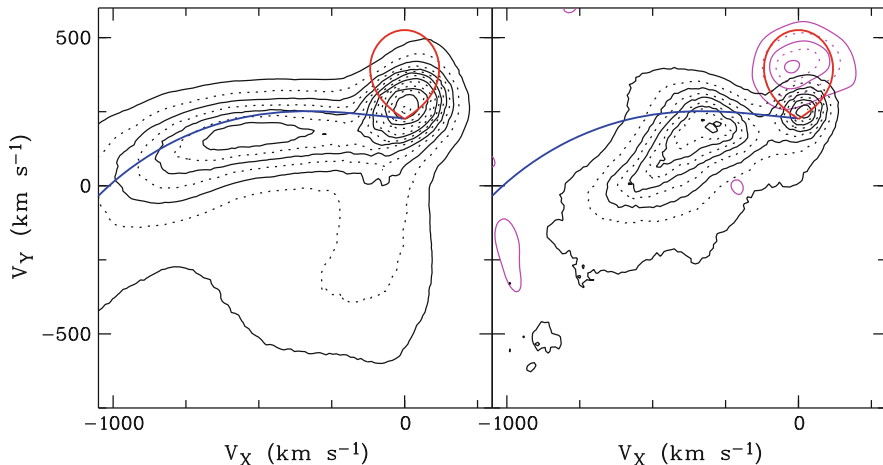


**Fig. 11.12** Shape of the Roche-lobe and location of the ballistic stream in Doppler coordinates for the best-known binary parameters of HU Aqr compared with Doppler maps of the HeII  $\lambda$  4685 obtained in high (*left*) and intermediate states of accretion. Shown in *magenta* is the Doppler map of the Na-doublet at 8183/9194 obtained simultaneously

of the two stars: the position of the donor star and of the ballistic stream. Can those be used to measure the masses of the stars in the binary?

Perhaps this is possible in principle, but in practice it turned out to be very difficult. The radius of the white dwarf could be measured with high signal-to-noise ratio with ULTRACAM at the VLT and the mass estimated using a mass-radius relationship. The radial velocity of the two hemispheres of the donor star were measured using Na absorption lines originating from the non-irradiated and Ca II emission lines from the irradiated hemispheres, respectively. This set of measurements constrains the mass ratio to  $Q = M_{\text{wd}}/M_2 = 4.6 \pm 0.2$ , the mass of the white dwarf to about  $0.8 M_{\odot}$ , and the inclination to  $87^\circ$ . The shape of the Roche lobe and the location of the ballistic stream are overlaid over the Doppler maps in Fig. 11.12.

In the high state the bulk of emission from the 'ballistic' accretion stream does not follow the single-particle trajectory but is displaced by  $60\text{--}70 \text{ km s}^{-1}$  towards negative  $v_y$ . A mass ratio of about 2.5 would be needed to give a best match between the model and the observation, which is impossible to achieve given the other observational constraints. In both maps there is a considerable amount of emission also at higher positive  $v_y$  velocities which is difficult to understand given the well-known accretion geometry of HU Aqr as sketched in Fig. 11.10. The high inclination of the object rules out  $v_z$ -effects as a possible interpretation. Also, the free-falling accretion stream is thought to be incompressible, hence one expects no velocity broadening perpendicular to the streaming direction (see the model maps for this object by [16]).

While the use of the He II Doppler maps cannot be used directly for a determination of the binary star parameters, they offer deep insight into the flow pattern in the binary. While the high state ballistic stream stretches to  $V_x < -1000 \text{ km s}^{-1}$ , it is stopped at  $V_x \simeq -600 \text{ km s}^{-1}$  at reduced accretion rate. Hence, the stream does not reach the same high-infall velocities along the ballistic part before it is overcome by the magnetic pressure. Hence the reduction in the mass accretion rate leads to a reduction in the mass density. The stream then seems to be re-directed so that it appears in the lower left quadrant in Doppler coordinates. There it occupies rather different regions in the two accretion states. This reflects that accretion happens along different field lines in different accretion states. Extended phases of absorption in the soft X-ray light curves reveal the existence of an extended accretion curtain, which is spanned between the inner Lagrangian point and the magnetically guided accretion streams that transports the bulk of the accreting matter. Ionisation and re-emission will happen all along the accretion curtain and reveals broad structures in the region of the Doppler maps to the lower-left of the ballistic trajectory. Attempts were made to map the brightness distribution along the accretion stream with and without velocity information [13, 15, 59].

UZ For is in many respects a twin system of HU Aqr as far as the orbital period and the X-ray properties are concerned. Its trailed spectrogram and the resulting Doppler map for He II 4685 are shown in Fig. 11.13. As in HU Aqr, there is an apparently clear indication of a ballistic stream reaching a maximum free-fall velocity of  $v_x \simeq -650 \text{ km s}^{-1}$ . The stream is then re-directed into the lower left quadrant where it still can be found as a rather well-focused structure. The overlaid streams in the right panel of the Figure were computed for matter streaming along dipolar field lines and allowed to determine the orientation of the magnetic axis (azimuth  $\varphi = 45^\circ$ , co-latitude  $\beta = 15^\circ$ ).

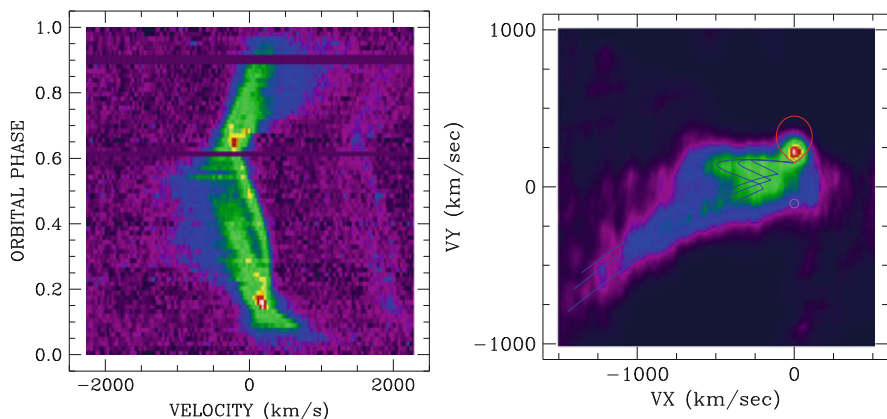


**Fig. 11.13** Trailed spectrogram (HeII $\lambda$ 4685, folded into 70 phase bins) and Doppler map of the  $P_{\text{orb}} = 126.5$  min eclipsing polar UZ For

The trajectories in Fig. 11.13 were computed for a mass ratio  $Q = M_{\text{wd}}/M_2 = 3$ . If the donor star followed Knigge’s sequence, it would have a mass  $M_2 = 0.19 M_{\odot}$  [23, 24]. The two numbers imply an undermassive white dwarf (see the recent compilation by [10]). As discussed in [32] a high-speed, high S/N low-state light curve, which would allow to measure the radius of the white dwarf directly, is still missing but current high-state photometry already gives strong evidence for a more massive white dwarf with  $M_{\text{wd}} \simeq 0.74 M_{\odot}$ . Hence, the two apparently cleanest examples for Doppler maps with matter freely falling along single-particle trajectories are in disagreement with mass ratio measurements and thus challenging our understanding of both the ionisation processes and the dynamics of the accretion stream.

The long-period polar QQ Vul shows even more complexities of those emission patterns by displaying a time-dependent shift of the  $v_y$  velocity of the putative “ballistic” trajectory [41]. There is no obvious reason for such a displacement. However, the observation of an almost stationary NV line in AM Her which was interpreted as being due to matter in a magnetic slingshot prominence emanating from the secondary star [11] may be stimulating thoughts about models with other magnetic structures, perhaps even those with open field lines that may exist in the vicinity of  $L_1$  and that eventually acts as venting system for matter to be released towards the white dwarf. Currently it seems difficult if not impossible to uniquely locate the single-particle trajectory of freely falling matter from  $L_1$  into the Roche lobe of the white dwarf.

### 11.4.2 Accretion Curtains in Asynchronous Polars

Most polars display just one period, which means that the spin of the white dwarf and the orbit are truly locked. A small subgroup of just five objects however shows a small asynchronism of a percent or less between those two quantities, the reported synchronisation time scales are  $10^2 \dots 10^3$  years.

The first tomographic analysis of such a system, BY Cam, revealed line emission spread out over a large velocity range forming a crescent at negative  $v_y$  velocities in the Doppler maps (see Fig. 11.14, adapted from [40]). This was regarded as evidence that the majority of the matter is accreted via an extended curtain. Location and extent of the structure in the Doppler maps could be reproduced with a simple curtain model raised over a wide ( $\sim 180^\circ$ ) range in azimuth implying that the ballistic stream stretches to a point far behind the white dwarf.

Figure 11.14 also shows a Doppler map of the only eclipsing asynchronous polar, V1432 Aql, based on VLT/FORS longslit spectroscopy. Data covering 2.3 binary cycles of the long-period polar,  $P_{\text{orb}} = 3.4$  h, were continuum-subtracted and phase-averaged for the creation of the Doppler map. The orbital inclination of BY Cam is moderate, the map thus might be affected by the  $v_z$  effects described above. They do not play a role in V1432 Aql. The spread of emission predominantly into the two lower quadrants in the Doppler map of this system therefore is real.

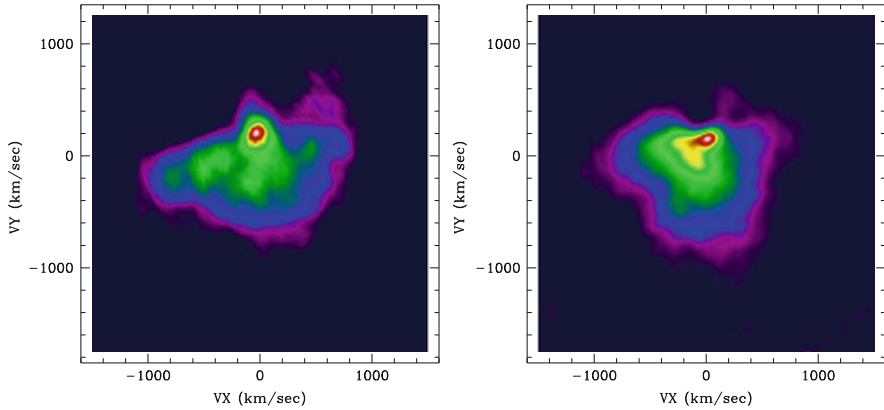


**Fig. 11.14** Doppler maps of the asynchronous polars BY Cam ( $H\beta$ , *left*) and V1432 Aql (He II 4685, *right*)

One observes large velocities in negative  $y$ -direction over a wide range of positive and negative  $v_x$ -velocities. Similarly to BY Cam, the map may be interpreted by an azimuthally extended accretion curtain. Emission from matter up to an azimuth of  $180^\circ$  is required to explain the negative  $v_y$ -velocity component at all velocities  $v_x$ . Emission in the upper right quadrant, i.e. positive velocities in both projected velocity components, is suggestive of matter that has made it around the white dwarf to an azimuth of up to  $270^\circ$  and being accreted at the far side of the white dwarf. However, a proper interpretation of the maps requires support from hydrodynamical models of the accretion flow in asynchronous polars.

### 11.4.3 The Donor Stars

The donor stars in polars could be traced and measured by the narrow emission lines originating in a quasi-chromosphere from the EUV-irradiated part of those stars (examples are shown in Figs. 11.9 and 11.13) and through photospheric absorption lines. Long-period polars are harbouring larger and hotter, thus brighter donors than their short-period brothers. Objects above the CV period gap thus may show emission and absorption lines even in their high accretion states. Below the period gap one typically needs a low state to uncover photospheric radiation from the donors while below  $P_{\text{orb}} \sim 110$  min the donors become too faint and are always outshone by accretion-induced radiation or even by the white dwarfs. Examples for long-period objects with Doppler maps based on photospheric absorption lines are V1309 Ori, AM Her, and QQ Vul [7, 49, 50]. HU Aqr is a very good example for a short-period object with both, emission and absorption lines [43] and EF Eridani for a polar showing only emission lines from its irradiated substellar secondary [42].



The immediate use of the emission lines lies in the ability to measure the orbital period unequivocally and to locate all other observed features with respect to true phase zero, i.e. with respect to the line joining both stars in the binary. While this may be achieved easily in low-state objects via Gaussian fits to line profiles and sine-fits to the radial velocity curves of the NEL, high-state objects and in particular the asynchronous polars reveal the location of the donor stars only in their Doppler maps.

When looking at the donor stars not all points are equally visible at all times. This violation of another axiom of Doppler tomography was motivating the development of Roche tomography (see [60], and the following chapter in this book). Some important conclusions as well as complexities and potential limitations of Roche tomography can nevertheless be derived from straight Doppler tomography, in particular if the narrow emission lines (NEL) from the irradiated hemisphere are concerned. There is no doubt that the NEL in various objects is a tracer of the donor, but its exact location is a variable. Lines of different atomic species may show different radial velocity amplitudes at a given epoch, hence appear at different  $v_y$  (Fig. 11.15). Lines of the same atomic species may show different radial velocity amplitudes at different epochs (Fig. 11.9). The size of these effects hasn't been investigated systematically but will depend on the irradiation spectrum and the distribution of gaseous matter around the  $L_1$ -point. This becomes obvious from, e.g., the He II maps in HU Aqr (Figs. 11.9 and 11.12), which always show their peak emission at the trailing side of the donor star due to shielding of the leading side by an accretion curtain. This also means that the radial velocity curves of those lines have a small but non-negligible phase-shift with respect to true phase zero.

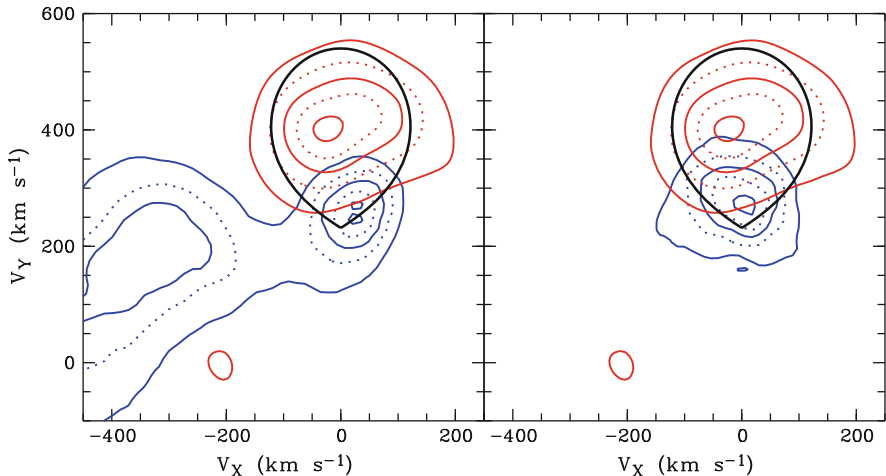


**Fig. 11.15** Doppler maps of He II 4686 emission and Na I 8194 absorption lines (*left panel*, shown with *blue* and *red* contours, respectively) and Ca II 8498 emission plus Na I 8194 absorption lines (*right panel*) obtained in a high state of HU Aqr. The size of the Roche lobe corresponds to  $Q = M_{\text{wd}}/M_2 = 4.58$  [43]



Thus, if it comes to mass estimates based on the emission lines (with an appropriate  $K$ -correction) it is recommended to use preferentially the Ca II triplet both in magnetic and non-magnetic cataclysmic variables [5, 58]. The low Ca I ionisation potential of 6.1 eV, lower than the ionisation potential of hydrogen, seems to ensure full and mainly unshielded irradiation of the secondary, while the ionising photons causing H and He emission have to pass an accretion curtain or other structures which may lead to a very complex irradiation pattern.

Kafka et al. [21, 22] reported the occurrence of satellite lines to H $\alpha$  in the low states of five polars. Their location in the Doppler maps at high positive  $v_y$ -velocities and close to the Roche lobes of the donor star were interpreted as being of magnetic origin in the form of large loops being fed with prominence-like material released from the active donor star (for an illustration of a similar structure in AM Her see [49], while for further reports of sling-shot prominences see [11, 48, 54, 61]). It appears that those structures might stay in place for times significantly longer than the lifetimes of prominences in single fast rotating stars. [22] argue that the magnetic interaction of the two stellar components acts as a stabilising element.

#### 11.4.4 Summary on Polars

Doppler tomography of magnetic CVs has uncovered structures as small as  $0.1 R_{\odot}$  at distances as large as a few 100 pc. The resolution thus achieved is below the micro-arcsec scale. It has made visible the accretion streams in the strongly magnetic CVs called polars, it has uncovered the existence of accretion curtains and structures on or associated with the donor stars in this type of CVs. The interpretation of the Doppler maps is still not fully developed and needs theoretical support.

## References

1. Agafonov, M., Richards, M., Sharova, O.: Three-dimensional Doppler tomogram of gas flows in the Algol-type binary U Coronae Borealis. *ApJ* **652**, 1547 (2006)
2. Agafonov, M.I., Sharova, O.I.: Few projections astrotomography: radio astronomical approach to 3D reconstruction. *Astronomische Nachrichten* **326**, 143 (2005)
3. Baba, H., Sadakane, K., Norimoto, Y., Ayani, K., Ioroi, M., Matsumoto, K., Nogami, D., Makita, M., Taichi, K.: Spiral structure in WZ Sagittae around the 2001 outburst maximum. *PASJ* **54**, L7 (2002)
4. Bassa, C.G., Jonker, P.G., Steeghs, D., Torres, M.A.P.: Optical spectroscopy of the quiescent counterpart to EXO0748-676. *MNRAS* **399**, 2055 (2009)
5. Beuermann, K., Reinsch, K.: High-resolution spectroscopy of the intermediate polar EX Hydrae. I. Kinematic study and Roche tomography. *A&A* **480**, 199 (2008)
6. Casares, J., Steeghs, D., Hynes, R.I., Charles, P.A., O'Brien, K.: Bowen fluorescence from the companion star in X1822-371. *ApJ* **590**, 1041 (2003)

7. Catalán, M.S., Schwope, A.D., Smith, R.C.: Mapping the secondary star in QQ Vulpeculae. *MNRAS* **310**, 123 (1999)
8. Diaz, M.P., Steiner, J.E.: Locating the emission line regions in polars: Doppler imaging of VV Puppis. *A&A* **283**, 508 (1994)
9. Echevarría, J.: Doppler tomography in cataclysmic variables: an historical perspective. *Mem. Soc. Astron. Ital.* **83**, 570 (2012)
10. Ferrario, L., de Martino, D., Gänsicke, B.T.: Magnetic white dwarfs. *Space Sci. Rev.* (2015)
11. Gänsicke, B.T., Hoard, D.W., Beuermann, K., Sion, E.M., Szkody, P.: HST/GHRS observations of AM Herculis. *A&A* **338**, 933 (1998)
12. Groot, P.J.: Evolution of spiral shocks in U Geminorum during outburst. *ApJ* **551**, L89 (2001)
13. Hakala, P., Cropper, M., Ramsay, G.: 3D eclipse mapping in AM Herculis systems – ‘genetically modified fireflies’. *MNRAS* **334**, 990 (2002)
14. Harlaftis, E.T., Steeghs, D., Horne, K., Martín, E., Magazzú, A.: Spiral shocks in the accretion disc of IP Peg during outburst maximum. *MNRAS* **306**, 348 (1999)
15. Harrop-Allin, M.K., Hakala, P.J., Cropper, M.: Indirect imaging of the accretion stream in eclipsing polars – I. Method and tests. *MNRAS* **302**, 362 (1999)
16. Heerlein, C., Horne, K., Schwope, A.D.: Modelling of the magnetic accretion flow in HU Aquarii. *MNRAS* **304**, 145 (1999)
17. Horne, K.: Images of accretion discs. I – the eclipse mapping method. *MNRAS* **213**, 129 (1985)
18. Horne, K., Marsh, T.R., Cheng, F.H., Hubeny, I., Lanz, T.: HST eclipse mapping of dwarf nova OY Carinae in quiescence: an ‘Fe II curtain’ with Mach approx. = 6 velocity dispersion veils the white dwarf, *ApJ* **426**, 294 (1994)
19. Hutchings, J.B., Fisher, W.A., Cowley, A.P., Crampton, D., Liller, M.H.: The complex emission-line structure in the magnetic white dwarf binary 2A 0311-227 /EF Eridani/. *ApJ* **252**, 690 (1982)
20. Joergens, V., Spruit, H.C., Rutten, R.G.M.: Spirals and the size of the disk in EX Dra. *A&A* **356**, L33 (2000)
21. Kafka, S., Ribeiro, T., Baptista, R., Honeycutt, R.K., Robertson, J.W.: New complexities in the low-state line profiles of AM Herculis. *ApJ* **688**, 1302 (2008)
22. Kafka, S., Tappert, C., Ribeiro, T., Honeycutt, R.K., Hoard, D.W., Saar, S.: Low-state magnetic structures in polars: nature or nurture? *ApJ* **721**, 1714 (2010)
23. Knigge, C.: The donor stars of cataclysmic variables. *MNRAS* **373**, 484 (2006)
24. Knigge, C.: Erratum: the donor stars of cataclysmic variables. *MNRAS* **382**, 1982 (2007)
25. Kononov, D.A., Agafonov, M.I., Sharova, O.I., Bisikalo, D.V., Zhilkin, A.G., Sidorov, M.Y.: The applicability of 3D Doppler tomography to studies of polars. *Astron. Rep* **58**, 881 (2014)
26. Kraft, R.P., Mathews, J., Greenstein, J.L.: Binary stars among cataclysmic variables. II. Nova WZ Sagittae: a possible radiator of gravitational waves. *ApJ* **136**, 312 (1962)
27. Marsh, T.R.: Kinematics of the helium accretor GP COM. *MNRAS* **304**, 443 (1999)
28. Marsh, T.R.: Doppler tomography. In: Boffin, H.M.J., Steeghs, D., Cuypers, J. (eds.) *Astro-tomography, Indirect Imaging Methods in Observational Astronomy. Lecture Notes in Physics*, vol. 573, p. 1. Springer, Berlin (2001)
29. Marsh, T.R.: Doppler tomography. *Ap&SS* **296**, 403 (2005)
30. Marsh, T.R., Horne, K.: Images of accretion discs. II – Doppler tomography. *MNRAS* **235**, 269 (1988)
31. Morales-Rueda, L., Marsh, T.R., Steeghs, D., Unda-Sanzana, E., Wood, J.H., North, R.C.: New results on GP Com. *A&A* **405**, 249 (2003)
32. Perryman, M.A.C., Cropper, M., Ramsay, G., Favata, F., Peacock, A., Rando, N., Reynolds, A.: High-speed energy-resolved STJ photometry of the eclipsing binary UZ For. *MNRAS* **324**, 899 (2001)
33. Richards, M.T., Agafonov, M.I., Sharova, O.I.: New evidence of magnetic interactions between stars from three-dimensional Doppler tomography of Algol binaries:  $\beta$  PER and RS VUL. *ApJ* **760**, 8 (2012)

34. Richards, M.T., Sharova, O.I., Agafonov, M.I.: Three-dimensional Doppler tomography of the RS Vulpeculae interacting binary. *ApJ* **720**, 996 (2010)
35. Roelofs, G.H.A., Groot, P.J., Marsh, T.R., Steeghs, D., Barros, S.C.C., Nelemans, G.: SDSS J124058.03-015919.2: a new AM CVn star with a 37-min orbital period. *MNRAS* **361**, 487 (2005)
36. Roelofs, G.H.A., Groot, P.J., Nelemans, G., Marsh, T.R., Steeghs, D.: Kinematics of the ultracompact helium accretor AM canum venaticorum, *MNRAS* **371**, 1231 (2006)
37. Roelofs, G.H.A., Rau, A., Marsh, T.R., Steeghs, D., Groot, P.J., Nelemans, G.: Spectroscopic evidence for a 5.4 min orbital period in HM cancri. *ApJ* **711**, L138 (2010)
38. Rosen, S.R., Mason, K.O., Cordova, F.A.: Phase-resolved optical spectroscopy of the AM HER system E1405-451. *MNRAS* **224**, 987 (1987)
39. Savoury, C.D.J., Littlefair, S.P., Dhillon, V.S., Marsh, T.R., Gänsicke, B.T., Copperwheat, C.M., Kerry, P., Hickman, R.D.G., Parsons, S.G.: Cataclysmic variables below the period gap: mass determinations of 14 eclipsing systems. *MNRAS* **415**, 2025 (2011)
40. Schwarz, R., Schwöpe, A.D., Staude, A., Remillard, R.A.: Doppler tomography of the asynchronous polar BY Camelopardalis, *A&A* **444**, 213 (2005)
41. Schwöpe, A.D., Catalán, M.S., Beuermann, K., Metzner, A., Smith, R.C., Steeghs, D.: Multi-epoch Doppler tomography and polarimetry of QQ Vul. *MNRAS* **313**, 533 (2000)
42. Schwöpe, A.D., Christensen, L.: X-shooting EF Eridani: further evidence for a massive white dwarf and a sub-stellar secondary. *A&A* **514**, A89 (2010)
43. Schwöpe, A.D., Horne, K., Steeghs, D., Still, M.: Dissecting the donor star in the eclipsing polar HU Aquarii. *A&A* **531**, A34 (2011)
44. Schwöpe, A.D., Mantel, K.H., Horne, K.: Phase-resolved high-resolution spectrophotometry of the eclipsing polar HU Aquarii. *A&A* **319**, 894 (1997)
45. Schwöpe, A.D., Staude, A., Vogel, J., Schwarz, R.: Indirect imaging of polars. *Astronomische Nachrichten* **325**, 197 (2004)
46. Simon, K.P., Sturm, E.: Disentangling of composite spectra. *A&A* **281**, 286 (1994)
47. Skilling, J., Bryan, R.K.: Maximum entropy image reconstruction – general algorithm. *MNRAS* **211**, 111 (1984)
48. Southworth, J., Marsh, T.R., Gänsicke, B.T., Steeghs, D., Copperwheat, C.M.: Orbital periods of cataclysmic variables identified by the SDSS. VIII. A slingshot prominence in SDSS J003941.06+005427.5? *A&A* **524**, A86 (2010)
49. Staude, A., Schwöpe, A.D., Hedelt, P., Rau, A., Schwarz, R.: Tomography of AM Her and QQ Vul. In: Vriellmann, S., Cropper, M. (eds.) *IAU Colloq. 190: Magnetic Cataclysmic Variables*. Astronomical Society of the Pacific Conference Series, vol. 315, p. 251. Astronomical Society of the Pacific, San Francisco (2004)
50. Staude, A., Schwöpe, A.D., Schwarz, R.: System parameters of the long-period polar V1309 Ori. *A&A* **374**, 588 (2001)
51. Steeghs, D.: Extending emission-line Doppler tomography: mapping-modulated line flux. *MNRAS* **344**, 448 (2003)
52. Steeghs, D., Casares, J.: The mass donor of scorpion X-1 revealed. *ApJ* **568**, 273 (2002)
53. Steeghs, D., Harlaftis, E.T., Horne, K.: Spiral structure in the accretion disc of the binary IP Pegasi. *MNRAS* **290**, L28 (1997)
54. Steeghs, D., Horne, K., Marsh, T.R., Donati, J.F.: Slingshot prominences during dwarf nova outbursts? *MNRAS* **281**, 626 (1996)
55. Steeghs, D., Marsh, T., Knigge, C., Maxted, P.F.L., Kuulkers, E., Skidmore, W.: Emission from the secondary star in the old cataclysmic variable WZ Sagittae. *ApJ* **562**, L145 (2001)
56. Stover, R.J.: A radial-velocity study of the dwarf nova RU Pegasi. *ApJ* **249**, 673 (1981)
57. Uemura, M., Kato, T., Nogami, D., Mennickent, R.: Doppler tomography by total variation minimization. *PASJ* **67**, 22 (2015)

58. van Spaandonk, L., Steeghs, D., Marsh, T.R., Torres, M.A.P.: Time-resolved spectroscopy of the pulsating CV GW Lib. *MNRAS* **401**, 1857(2010)
59. Vrielmann, S., Schwope, A.D.: Accretion stream mapping of HU Aquarii. *MNRAS* **322**, 269 (2001)
60. Watson, C.A., Dhillon, V.S.: Roche tomography of cataclysmic variables – I. Artefacts and techniques. *MNRAS* **326**, 67 (2001)
61. Watson, C.A., Steeghs, D., Shahbaz, T., Dhillon, V.S.: Roche tomography of cataclysmic variables – IV. Star-spots and slingshot prominences on BV Cen. *MNRAS* **382**, 1105 (2007)